Organic Photovoltaic Devices Using Highly Flexible Reduced Graphene Oxide Films as Transparent Electrodes

Zongyou Yin,[†] Shuangyong Sun,[†] Teddy Salim,[†] Shixin Wu,[†] Xiao Huang,[†] Qiyuan He,[†] Yeng Ming Lam,[†,*] and Hua Zhang[†,‡,*]

[†]School of Materials Science and Engineering, Nanyang Technological University, 50 Nanyang Avenue, Singapore 639798 and [‡]Centre for Biomimetic Sensor Science, Nanyang Technological University, 50 Nanyang Drive, Singapore 637553

ABSTRACT The chemically reduced graphene oxide (rGO) was transferred onto polyethylene terephthalate (PET) substrates and then used as transparent and conductive electrodes for flexible organic photovoltaic (OPV) devices. The performance of the OPV devices mainly depends on the charge transport efficiency through rGO electrodes when the optical transmittance of rGO is above 65%. However, if the transmittance of rGO is less than 65%, the performance of the OPV device is dominated by the light transmission efficiency, that is, the transparency of rGO films. After the tensile strain (~2.9%) was applied on the fabricated OPV device, it can sustain a thousand cycles of bending. Our work demonstrates the highly flexible property of rGO films, which provide the potential applications in flexible optoelectronics.

KEYWORDS: reduced graphene oxide · organic photovoltaic devices · flexible electrodes · optical transmittance · bending-induced tensile stress

As one of the solar energy harvesting platforms, polymer-based organic photovoltaic (OPV) devices have attracted increasing attention in both scientific and industrial communities due to their unique characteristics, such as low cost, solution-based process, light weight, and compatibility with flexible substrates.[1−3] Great progress on OPV devices has been achieved since the report published by Tang *et al.*[4] The improvement of device structures and fabrication techniques has enabled an overall power conversion efficiency as high as ~7%, obtained in the OPV devices with the bulk heterojunction (BHJ)-based active layers.[5−12] In these devices, the transparent conductive electrode, used to couple photons into the active layers, is extensively the indium tin oxide (ITO). However, the use of such metal oxides seems to be increasingly problematic due to the limited indium source, their susceptibility to ion diffusion into polymer layers, their instability in acid or base, and the brittle nature of metal oxide.[13−17]

The two-dimensional (2D) single-layer honeycomb-latticed carbon material, graphene, has emerged as a rising star in the field of materials. Owing to its unique electrical, chemical, and mechanical properties, graphene has been developed for various applications in field-effect transistors (FETs),[18−21] sensors,[22−27] memories,[28−32] biology,[33,34] electrochemistry,[35,36] and optoelectronics.[37,38] Meanwhile, many studies on graphene-based photovoltaic applications have been carried out, in which graphene was used as active layer materials,[39−41] electron transport bridges,[42−44] and transparent electrodes.[45−52] Particularly, owing to its flexibility, graphene has been reported to be sustainable within a certain range of tension/compression force.[53−56] Therefore, it is important to explore the flexible behavior of graphene in photovoltaics. Unfortunately, to date, there are rare studies that report the use of flexible graphene films on the polyethylene terephthalate (PET) substrates as transparent electrodes in the photovoltaic devices. For example, Arco *et al.* transferred the chemical vapor deposition (CVD)-grown graphene onto the PET substrate for OPV applications.[45] However, the preparation of graphene through CVD and active layers through thermal evaporation results in the high cost in the device fabrication.

In this contribution, the highly conductive, chemically reduced graphene oxide (rGO) film was transferred onto a PET substrate, referred to as rGO/PET, which was then used as a transparent electrode for the OPV devices. The active layer of the device was prepared by a simple and low-cost spin-coating method. As observed, the device performance is dependent on the charge transport efficiency from the active layer to rGO electrode, and it is not sensitive to transmittance of rGO electrode (if >65%).

*Address correspondence to hzhang@ntu.edu.sg, ymlam@ntu.edu.sg.

Received for review July 9, 2010 and accepted August 16, 2010.

Published online August 25, 2010. 10.1021/nn1015874

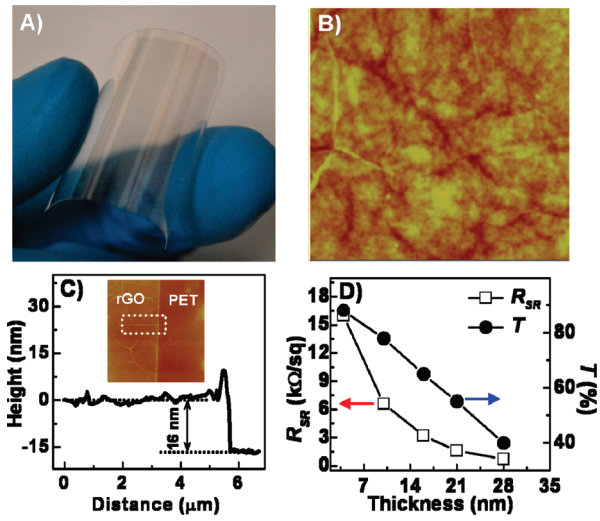

Figure 1. (A) Photograph of rGO/PET. (B) AFM topographic image (3 × 3 μm²) of rGO/PET. (C) AFM image and section analysis of 16 nm thick rGO film on PET; *i.e.*, rGO/PET in panel B. (D) Sheet resistance (R_{SR}) and transmittance (T) of rGO film as a function of its thickness.

As a result, lowering the rGO sheet resistance *via* increasing the rGO thickness notably enhances the current density of devices and thus the overall power conversion efficiency (η), even if the transmittance of rGO film decreases. The highest η obtained in the flexible rGO/PET-based OPV devices is 0.78%. These devices show an excellent stability after applying the bending-induced tension stress, and their performance can be well maintained even after bending a thousand times.

RESULTS AND DISCUSSION

Preparation and Characterization of rGO Films on PET. With some modification of the previously reported method, which was used to transfer rGO films from SiO_2/Si to PET substrates,[55,57] we prepared the flexible, transparent rGO/PET electrodes. The detailed process is given in the Materials and Methods. Figure 1A shows the photograph of the made flexible rGO/PET, which could be bent to a certain angle. The atomic force microscope (AFM) image of a typical rGO/PET is shown in Figure 1B. The obtained root-mean-square (rms) roughness of 3 × 3 μm² rGO film is ~3 nm. Thickness of rGO film can be measured by AFM (*e.g.*, 16 nm as shown in Figure 1C). The correlation of sheet resistance (R_{SR}) and transmittance (T) at 550 nm of rGO film to its thickness is plotted in Figure 1D. The obtained lowest R_{SR} is 720 Ω/sq for the 28 nm thick rGO, whose transmittance is ~40%. The highest optical transmittance, 88%, was obtained in the 4 nm thick rGO, but the sheet resistance dramatically increased to 16.0 kΩ/sq. These results are similar to the previous report.[57]

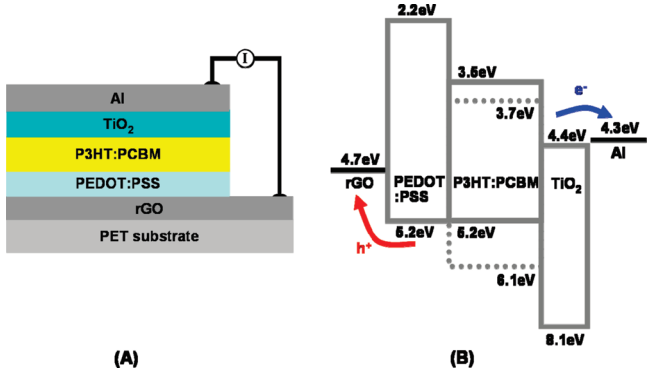

Figure 2. Schematic representation of (A) the layer structure and (B) energy level for the OPV device, *i.e.*, rGO/PEDOT:PSS/P3HT:PCBM/TiO_2/Al, with rGO as the transparent electrode.

Performance of rGO/PET-Based OPV Devices. All of the OPV devices were fabricated on the flexible, transparent, and conductive rGO/PET electrodes. The layered structure of the device and the corresponding energy level diagram are schematically shown in Figure 2A, and B, respectively. In all devices, the blend of poly(3-hexylthiophene) (P3HT) and phenyl-C_{61}-butyric acid methyl ester (PCBM)-based bulk heterojunction (BHJ) was used as the active layer (100 nm). In order to enhance the hole transport efficiency from the highest occupied molecular orbital (HOMO) level of P3HT to the rGO anode by blocking the electrons and then reducing the recombination of electrons and holes at the interface, a 10 nm thick hole transport layer of poly(3,4-ethylenedioxythiophene):poly(styrenesulfonate) (PEDOT:PSS) was sandwiched between the rGO electrode and BHJ active layer. Similarly, to block the holes and increase the electron transport from the lowest unoccupied molecular orbital (LUMO) of PCBM to the Al electrode, a thin layer of TiO_2 nanoparticles was sandwiched between the BHJ active layer and Al electrode.

In order to study the effect of rGO thickness on the performance of OPV devices, rGO films with different thickness were prepared on PET for OPV devices, for example, 4 nm (device 1), 10 nm (device 2), 16 nm (device 3), and 21 nm (device 4). The measured $J-V$ curves of the fabricated four OPV devices are shown in Figure 3. The photovoltaic performance of these devices has been summarized in Table 1. The four devices with different thickness of rGO films give the comparable open-circuit voltages (V_{oc}) of ~0.56 V, which is reasonable because V_{oc} is governed by the energetic relationship between the donor and acceptor in the BHJ-based OPV devices.[3,58,59] In this work, the active layer of the four devices is composed of P3HT:PCBM (donor:acceptor) BHJ fabricated in the same conditions. The fill factor (FF) of our devices shows a slight increase from device 1 (30%) to device 4 (32%), which is due to the reduction of sheet resistance when the thickness of rGO film increases. However, from device 1 to device 3, with an increase of the rGO thickness, the current density, J_{sc}, obviously increases from 1.74 to 4.39 mA/cm², directly resulting in a great enhancement of η from 0.28 to 0.78%, as shown in Table 1. It is worth noting that J_{sc} and η do not increase further even if the rGO thickness continuously increases (from device 3 to device 4). Therefore, there is an optimal rGO thickness to the

OPV performance. The overall power conversion efficiency in device 3 reaches 0.78%, which is still lower than 1.18% from the CVD-graphene/PET-based OPV devices, which is due to the lower sheet resistance and higher optical transmittance of the CVD-grown graphene,[45] compared with our chemically derived rGO film. The relation of device performance to rGO electrode as observed in this study is determined by two factors, that is, the sheet resistance of rGO electrode (determining the carrier transport efficiency) and the transparency of rGO (determining the light transmission efficiency). At the high transmittance of rGO film (*e.g.*, >65%), J_{sc} is no longer sensitive to rGO transmittance. Instead, it becomes more dependent on the sheet resistance of rGO; that is, J_{sc} increases with a decrease of sheet resistance (from device 1 to device 3 in Table 1). The smaller sheet resistance of rGO film benefits the carriers being pumped out from the device's BHJ active layer to rGO electrode. In terms of rGO-based devices, it is believed that the hole pumping-out efficiency from the HOMO level of P3HT to the rGO anode primarily determines the device overall performance. This is because the cathodes of the devices is aluminum, which has several orders lower sheet resistance (~0.4 Ω/sq for 70 nm thick Al electrode) than rGO film. The dependence of device performance on charge transport capacity from active layer to electrode, instead of how much efficiency of light coupling into device active layer, was also observed in the CVD-graphene-based OPV devices.[45] On the other hand, when the rGO film becomes too thick (*e.g.*, device 4), too low optical transmittance weakens the light transmission efficiency through the thick rGO film. This reduces the light-excited electron−hole pairs in the BHJ active layer and lowers the supply of electron/hole carriers for the external circuit, thus suppressing the device performance improvement from device 3 to device 4 (Table 1). Therefore, an optimal experimental condition must be made between the carrier pumping-out (determined by rGO sheet resistance) and light coupling-in (determined by rGO transparency) efficiency in the design of OPV devices, in order to maximize the performance of the devices with rGO transparent electrodes.

Bending Effect on Performance of rGO/PET-Based OPV Devices. The effect of mechanical property of rGO films on the performance of OPV devices was studied by monitoring the performance after applying tensile stress on the devices. The bending−relaxing experiments are shown in the insets of Figure 4A. In each cycle, the OPV device was first bent around a solid column (radius = 5 mm) and then fully relaxed immediately. Multiple cycles can be applied through the repetition of the bending and relaxing steps. The tensile strain is determined by the relatively extended length of rGO film under bending the underlying supporting PET substrate.[56] For the bending curvature with radius of 5 mm in our experiment, the tensile strain is calculated to be 2.9%. In this

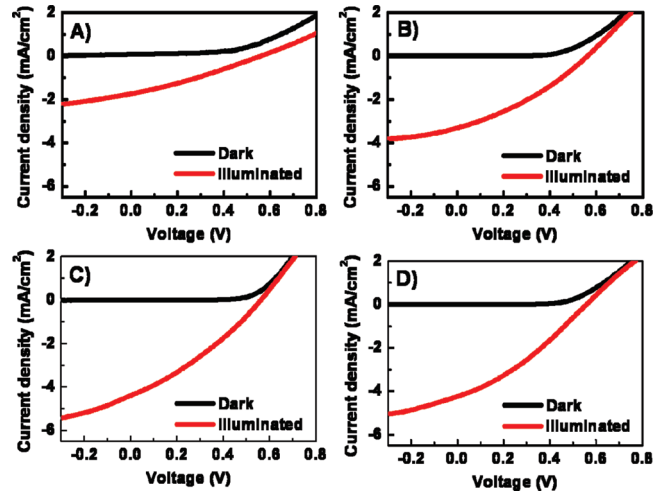

Figure 3. *J*−*V* curves of OPV devices on rGO/PET under 100 mW/cm² AM 1.5G simulated globe sun illumination with rGO film thickness of (A) 4 nm (device 1), (B) 10 nm (device 2), (C) 16 nm (device 3), and (D) 21 nm (device 4).

study, devices with two different rGO thicknesses (*i.e.*, devices 1 and 3 shown in Figure 3 and Table 1) were chosen for the bending−relaxing experiments. The *J*−*V* curves of the devices after a number of bending cycles are recorded. The typical *J*−*V* characteristics for device 1 after bending 400, 800, and 1200 times and device 3 after bending 800, 1200, and 1600 times are shown in Figure 4A, and B, respectively. As observed, the bending-induced variation of open-circuit voltages (V_{oc}) is negligible, and only a slight decrease of fill factor was observed after multiple bending (see Figure S1 in Supporting Information). This slight reduction of FF is probably induced by the degradation of interlayer contacts of the device. A significant decrease in J_{sc} and η was observed after certain bending cycles, which is dependent on the thickness of rGO film as discussed below.

The plots of J_{sc}, η, and R_{SR} of the rGO electrodes as a function of bending cycles for devices 1 and 3 are shown in Figure 4C, and D, respectively. The value of J_{sc} remains constant for certain bending cycles followed by a sudden drop after that. The same trend is also observed for the value of η of the devices. Note that the critical number of bending cycles to trigger the degradation of device performance in devices 1 and 3 is different. In device 1, fabricated on a 4 nm thick rGO electrode, J_{sc} and η start to drop after around 600 bends,

TABLE 1. Summary of the Performance of OPV Devices 1−4 Shown in Figure 3: The Thickness (*d*), Sheet Resistance (R_{SR}), and Transmittance (*T*) of rGO Electrodes Are Also Listed

Device (*d*, R_{SR}, *T* of rGO)	J_{sc} (mA/cm²)	V_{oc} (V)	FF	η (%)
1 (4 nm, 16.0 kΩ/sq, 88%)	1.74	0.557	0.30	0.28
2 (10 nm, 6.6 kΩ/sq, 78%)	3.31	0.560	0.31	0.61
3 (16 nm, 3.2 kΩ/sq, 65%)	4.39	0.561	0.32	0.78
4 (21 nm, 1.6 kΩ/sq, 55%)	4.24	0.557	0.32	0.77

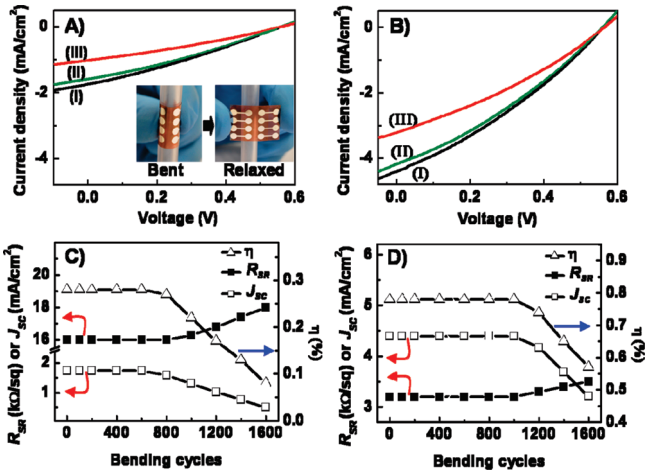

Figure 4. *J*−*V* curves of (A) device 1 (see Figure 3A) after applying (i) 400, (ii) 800, and (iii) 1200 cycles of bending, and (B) device 3 (see Figure 3C) after applying (I) 800, (II) 1200, and (III) 1600 cycles of bending. Note that the *J*−*V* curves of unbent device 1 and device 3 are not plotted because they are almost the same as curve i in (A) and curve I in (B), respectively. The short-circuit current density (J_{sc}), overall power conversion efficiency (η), and the sheet resistance (R_{SR}) of device 1 and device 3 are plotted as a function of bending cycles in (C) and (D), respectively. Inset in (A): photograph of the bending−relaxing experiments of the OPV device.

while device 3, with 16 nm thick rGO film, starts to show the drop of J_{sc} and η at more than 1000 bending cycles. This indicates the OPV device subjected to the tensile stress performs more stably when the rGO electrode is relatively thicker. The rGO film is composed of randomly stacked single-layer rGO sheets, which has good mechanic flexibility and can recover immediately after the strain relaxation.[56] However, the parallel overlapping/contacts between the 2D rGO sheets play a critical role in the rGO resistance. Frequent bending induces thermal effect, which results in the loosening of the overlapping/contacts between rGO sheets, thus increasing the sheet−sheet contact resistance and then the whole resistance of rGO films. In the thicker rGO film with more stacked rGO sheets, the probability to maintain the initial good sheet−sheet contacts and sheet resistance is higher, which enables it to withstand higher tensile stress. In order to confirm this point, the variation of sheet resistance has also been monitored for the pure rGO/PET under the same bending condition. The transmittance values were observed to be nearly constant for all rGO films before and after bending (Figure S2 in Supporting Information). However, the sheet resistance increased from 16.0 to 18.0 kΩ/sq and 3.2 to 3.5 kΩ/sq, respectively, for the 4 and 16 nm rGO films before and after 1600 bending cycles (Figure 4C,D). It indicates that the increase in R_{SR} value of rGO films after certain bending cycles gives the direct impairment on the device performance. This further demonstrates the dependence of the stability of device performance under tensile stress on the mechanic stability of the rGO film. For comparison, the OPV devices were also fabricated in the same conditions on the commercial ITO-coated PET wafers (bought from Sigma-Aldrich, measured R_{SR} = 120 Ω/sq), referred to as ITO/PET. However, the brittle nature of the ITO electrode leads to the obvious cracking of ITO film upon bending (see Figure S4D in the Supporting Information). This directly increased the R_{SR} value of ITO/PET, thus degrading the device performance dramatically, which was observed from the *J*−*V* curves in Figure S4A and the values of R_{SR}, J_{sc}, and η as the function of bending cycles in Figure S4B. Therefore, it is worth noting that the fact that 16 nm rGO-film-based OPV devices are able to sustain a thousand bending cycles (2.9% tensile strain) indicates the highly mechanical flexibility of chemically derived rGO films.

CONCLUSIONS

Flexible, chemically derived rGO film was successfully transferred onto PET and thus used as the transparent, conductive electrode for OPV devices. A high dependence of device performance on the sheet resistance of rGO film, which determines the charge transport efficiency, was observed if the optical transmittance of rGO film was above 65%. In the low optical transmittance of rGO film (<65%), the transparency of rGO film, which determines the light transmission efficiency, dominates the device performance. Upon application of the external tensile stress, the rGO-film-based OPV devices can sustain a thousand cycles of bending. This demonstrates the highly mechanical flexibility of chemically derived rGO thin films. Importantly, our study paves a way to develop rGO films for wide applications in future flexible organic optoelectronics.

MATERIALS AND METHODS

Preparation of rGO Films on PET Substrates. Graphene oxide (GO) in methanol was synthesized from graphite powder by a modified Hummers method.[60,61] A 0.2 mg/mL graphene oxide (GO) solution in methanol was spin-coated at 4000 rpm onto a precleaned SiO_2/Si substrate (Bonda Tech, Singapore) to form GO film. The thickness of obtained GO film can be controlled by the spin-coating conditions. Subsequently, thermal annealing in Ar/H_2 (v/v = 1:1) at 1000 °C for 2 h was applied to reduce the GO film, and the reduced graphene oxide (rGO) film on SiO_2/Si (*i.e.*, rGO/SiO_2/Si) was obtained. Then, ~300 nm thick polymethyl methacrylate (PMMA, Sigma-Aldrich) was coated on rGO/SiO_2/Si followed by annealing at 170 °C for 2 h to dry the PMMA film. Successively, SiO_2 was etched away in 2 M NaOH solution at 70 °C, and the PMMA-supported rGO film (*i.e.*, PMMA/rGO film) was obtained. After the 0.3 mm thick PET substrate (3M, USA) was cleaned in ethanol and Milli-Q water (18.2 MΩ · cm) followed by the O_2 plasma treatment to create the hydrophilic surface, the PMMA/rGO film was transferred onto PET and then carefully dried with N_2 gas. The hydrophilic PET surface benefits to make the PMMA/rGO film smooth during drying with N_2. The PMMA/rGO/PET was dried at 80 °C for 1 h before the top PMMA film was etched with acetone. Finally, the obtained flexible, transparent rGO/PET electrode was baked at 150 °C for 2 h before it was used for the OPV device fabrication.

AFM images were obtained using Dimension 3100 (Veeco, CA) in tapping mode with a Si tip (Veeco, resonant frequency, 320 kHz; spring constant, 42 N m^{-1}) under ambient conditions with a scanning rate of 1 Hz and scanning line of 512.

Fabrication of OPV Devices on rGO/PET. First, the prepared rGO/PET was treated with O_2 plasma to generate the hydrophilic surface of rGO. The PEDOT:PSS (Sigma-Aldrich) solution (filtered through a 0.45 μm PVDF filter) was spin-coated onto the plasma-treated rGO/PET at 3000 rpm for 60 s. The resulting PEDOT:PSS/rGO/PET was transferred into a N_2-purged glovebox and then baked at 140 °C for 10 min. The following steps for device fabrication were all processed in the glovebox. P3HT (Rieke Metals, 4002-EE highly regioregular) and PCBM were dissolved in 1,2-dichlorobenzene (*o*-DCB), that is, 10 mg of P3HT and 8 mg of PCBM dissolved 1 mL of *o*-DCB, to obtain the P3HT:PCBM mixed solution, which was spin-coated at 700 rpm on the top of PEDOT:PSS/rGO/PET to form the BHJ active layer. The obtained film was dried at room temperature for 45 min. Then the ~200 μL of homemade TiO_2 nanoparticle ethanolic solution was spin-coated onto the BHJ layer at 2000 rpm for 60 s to form the TiO_2 layer. The preparation of TiO_2 nanoparticles follows a previous report.[62] The TiO_2 sol was prepared by hydrolysis of titanium isopropoxide in a mixture of ethanol and HCl. After 10-fold dilution with ethanol, the obtained 3 mM TiO_2 sol was heated in an autoclave at 160 °C for 16 h to form the TiO_2 nanoparticles with the size of ~10 nm (see Figure S3 in Supporting Information). To complete the device fabrication, Al electrode was deposited onto the TiO_2 layer through thermal evaporation. Finally, 20 min annealing at 150 °C was applied to all devices before the characterization. All of the measurements of current density *versus* voltage (*J*−*V*) were carried out at ambient conditions, and the illuminated light intensity used during the measurements is kept at 100 mW/cm^2.

Acknowledgment. The authors gratefully acknowledge the financial support from AcRF Tier 1 and Tier 2 (RG 20/07) from MOE, CRP (NRF-CRP2-2007-01) from NRF, A*STAR SERC Grants (#092 101 0064) from A*STAR, and the Centre for Biomimetic Sensor Science at NTU in Singapore.

Supporting Information Available: Characterizations of TiO_2 nanoparticles, transparent conductive electrodes, and the fabricated OPV devices. This material is available free of charge *via* the Internet at http://pubs.acs.org.

REFERENCES AND NOTES

1. Scharber, M. C.; Mühlbacher, D.; Koppe, M.; Denk, P.; Waldauf, C.; Heeger, A. J.; Brabec, C. J. Design Rules for Donors in Bulk-Heterojunction Solar Cells−Towards 10% Energy-Conversion Efficiency. *Adv. Mater.* **2006**, *18*, 789–794.
2. Mayer, A. C.; Scully, S. R.; Hardin, B. E.; Rowell, M. W.; McGehee, M. D. Polymer-Based Solar Cells. *Mater. Today* **2007**, *10*, 28–33.
3. Thompson, B. C.; Frechet, J. M. J. Polymer−Fullerene Composite Solar Cells. *Angew. Chem., Int. Ed.* **2008**, *47*, 58–77.
4. Tang, C. W. Two-Layer Organic Photovoltaic Cell. *Appl. Phys. Lett.* **1986**, *48*, 183–185.
5. Liang, Y.; Xu, Z.; Xia, J.; Tsai, S.; Wu, Y.; Li, G.; Ray, C.; Yu, L. For the Bright Future−Bulk Heterojunction Polymer Solar Cell with Power Conversion Efficiency of 7.4%. *Adv. Mater.* **2010**, *22*, E135–E138.
6. Chen, H.; Hou, J.; Zhang, S.; Liang, Y.; Yang, G.; Yang, Y.; Yu, L.; Wu, Y.; Li, G. Polymer Solar Cells with Enhanced Open-Circuit Voltage and Efficiency. *Nat. Photon.* **2009**, *3*, 649–653.
7. Park, S. H.; Roy, A.; Beaupre, S.; Cho, S.; Coates, N.; Moon, J. S.; Moses, D.; Leclerc, M.; Lee, K.; Heeger, A. J. Bulk Heterojunction Solar Cells with Internal Quantum Efficiency Approaching 100%. *Nat. Photonics* **2009**, *3*, 297–303.
8. Moulé, A. J.; Meerholz, K. Controlling Morphology in Polymer−Fullerene Mixtures. *Adv. Mater.* **2008**, *20*, 240–245.
9. Peet, J.; Kim, J. Y.; Coates, N. E.; Ma, W. L.; Moses, D.; Heeger, A. J.; Bazan, G. C. Efficiency Enhancement in Low-Bandgap Polymer Solar Cells by Processing with Alkane Dithiols. *Nat. Mater.* **2007**, *6*, 497–500.
10. Li, G.; Shrotriya, V.; Huang, J.; Yao, Y.; Moriarty, T.; Emery, K.; Yang, Y. High-Efficiency Solution Processable Polymer Photovoltaic Cells by Self-Organization of Polymer Blends. *Nat. Mater.* **2005**, *4*, 864–868.
11. Ma, W.; Yang, C.; Gong, X.; Lee, K.; Heeger, A. J. Thermally Stable, Efficient Polymer Solar Cells with Nanoscale Control of the Interpenetrating Network Morphology. *Adv. Funct. Mater.* **2005**, *15*, 1617–1622.
12. Kim, K.; Liu, J.; Namboothiry, M. A. G.; Carroll, D. L. Roles of Donor and Acceptor Nanodomains in 6% Efficient Thermally Annealed Polymer Photovotaics. *Appl. Phys. Lett.* **2007**, *90*, 163511.
13. Schlatmann, A. R.; Floet, D. W.; Hilberer, A.; Garten, F.; Smulders, P. J. M.; Klapwijk, T. M.; Hadziioannou, G. Indium Contamination from the Indium-Tin-Oxide Electrode in Polymer Light-Emitting Diodes. *Appl. Phys. Lett.* **1996**, *69*, 1764–1766.
14. Scott, J. C.; Kaufman, J. H.; Brock, P. J.; DiPietro, R.; Salem, J.; Goitia, J. A. Degradation and Failure of MEH-PPV Light-Emitting Diodes. *J. Appl. Phys.* **1996**, *79*, 2745–2751.
15. Andersson, A.; Johansson, N.; Broms, P.; Yu, N.; Lupo, D.; Salaneck, W. R. Fluorine Tin Oxide as an Alternative to Indium Tin Oxide in Polymer LEDs. *Adv. Mater.* **1998**, *10*, 859–863.
16. Jansseune, T. Indium Price Soars as Demand for Displays Continues to Grow. *Comp. Semicond.* **2005**, *11*, 34–35.
17. Boehme, M.; Charton, C. Properties of ITO on PET Film in Dependence on the Coating Conditions and Thermal Processing. *Surf. Coat. Technol.* **2005**, *200*, 932–935.
18. Bai, J.; Zhong, X.; Jiang, S.; Huang, Y.; Duan, X. Graphene Nanomesh. *Nat. Nanotechnol.* **2010**, *5*, 190–194.
19. Jiao, L.; Zhang, L.; Wang, X.; Diankov, G.; Dai, H. Narrow Graphene Nanoribbons from Carbon Nanotubes. *Nature* **2009**, *458*, 877–880.
20. Novoselov, K. S.; Geim, A. K.; Morozov, S. V.; Jiang, D.; Zhang, Y.; Dubonos, S. V.; Grigorieva, I. V.; Firsov, A. A. Electric Field Effect in Atomically Thin Carbon Films. *Science* **2004**, *306*, 666–669.
21. Li, B.; Cao, X. H.; Ong, H. G.; Cheah, J. W.; Zhou, X. Z.; Yin, Z. Y.; Li, H.; Wang, J.; Boey, F. Y.C.; Huang, W.; *et al.* All-Carbon Electronic Devices Fabricated by Directly Grown Single-Walled Carbon Nanotubes on Reduced Graphene Oxide Electrodes. *Adv. Mater.* **2010**, *22*, 3058–3061.
22. Wang, Z.; Zhou, X.; Zhang, J.; Boey, F.; Zhang, H. Direct Electrochemical Reduction of Single-Layer Graphene Oxide and Subsequent Functionalization with Glucose Oxidase. *J. Phys. Chem. C* **2009**, *113*, 14071–14075.
23. Dan, Y. P.; Lu, Y.; Kybert, N. J.; Luo, Z. T.; Johnson, A. T. C. Intrinsic Response of Graphene Vapor Sensors. *Nano Lett.* **2009**, *9*, 1472–1475.
24. Fowler, J. D.; Allen, M. J.; Tung, V. C.; Yang, Y.; Kaner, R. B.; Weiller, B. H. Practical Chemical Sensors from Chemically Derived Graphene. *ACS Nano* **2009**, *3*, 301–306.
25. He, Q.; Sudibya, H. G.; Yin, Z.; Wu, S.; Li, H.; Boey, F.; Huang, W.; Chen, P.; Zhang, H. Centimeter-Long and Large-Scale Micropatterns of Reduced Graphene Oxide Films: Fabrication and Sensing Applications. *ACS Nano* **2010**, *4*, 3201–3208.
26. Dong, X.; Shi, Y.; Huang, W.; Chen, P.; Li, L.-J. Electrical Detection of DNA Hybridization with Single-Base Specificity Using Transistors Based on CVD-Grown Graphene Sheets. *Adv. Mater.* **2010**, *22*, 1649–1653.
27. He, S.; Song, B.; Li, D.; Zhu, C.; Qi, W.; Wen, Y.; Wang, L.; Song, S.; Fang, H.; Fan, C. A. Graphene Nanoprobe for Rapid, Sensitive, and Multicolor Fluorescent DNA Analysis. *Adv. Funct. Mater.* **2010**, *20*, 453–459.
28. Zhuang, X.; Chen, Y.; Liu, G.; Li, P.; Zhu, C.; Kang, E.; Noeh, K.; Zhang, B.; Zhu, J.; Li, Y. Conjugated-Polymer-Functionalized Graphene Oxide: Synthesis and Nonvolatile Rewritable Memory Effect. *Adv. Mater.* **2010**, *22*, 1731–1735.
29. Zheng, Y.; Ni, G.; Toh, C.; Zeng, M.; Chen, S.; Yao, K.;

Özyilmaz, B. Gate-Controlled Nonvolatile Graphene-Ferroelectric Memory. *Appl. Phys. Lett.* **2009**, *94*, 163505.
30. Liu, J.; Yin, Z.; Cao, X.; Zhao, F.; Ling, A.; Xie, L.; Fan, Q. L.; Boey, F.; Zhang, H.; Huang, W. Bulk Heterojunction Polymer Memory Devices with Reduced Graphene Oxide as Electrodes. *ACS Nano* **2010**, *4*, 3987–3992.
31. Myung, S.; Park, J.; Lee, H.; Kim, K. S.; Hong, S. Ambipolar Memory Devices Based on Reduced Graphene Oxide and Nanoparticles. *Adv. Mater.* **2010**, *22*, 2045–2049.
32. Liu, J.; Lin, Z.; Liu, T.; Yin, Z.; Zhou, X.; Chen, S.; Xie, L.; Boey, F.; Zhang, H.; Huang, W. Multilayer-Stacked, Low Temperature-Reduced Graphene Oxide Films: Preparation, Characterization and Application in Polymer Memory Devices. *Small* **2010**, *6*, 1536–1542.
33. Tang, Z.; Wu, H.; Cort, J. R.; Buchko, G. W.; Zhang, Y.; Shao, Y.; Aksay, I. A.; Liu, J.; Lin, Y. Constraint of DNA on Functionalized Graphene Improves Its Biostability and Specificity. *Small* **2010**, *6*, 1205–1209.
34. Qin, W.; Li, X.; Bian, W. W.; Fan, X. J.; Qi, J. Y. Density Functional Theory Calculations and Molecular Dynamics Simulations of the Adsorption of Biomolecules on Graphene Surfaces. *Biomaterials* **2010**, *31*, 1007–1016.
35. Lu, T.; Zhang, Y.; Li, H.; Pan, L.; Li, Y.; Sun, Z. Electrochemical Behaviors of Graphene–ZnO and Graphene–SnO_2 Composite Films for Supercapacitors. *Electrochim. Acta* **2010**, *55*, 4170–4173.
36. Kim, Y.; Bong, S.; Kang, Y.; Yang, Y.; Mahajan, R. K.; Kim, J. S.; Kim, H. Electrochemical Detection of Dopamine in the Presence of Ascorbic Acid Using Graphene Modified Electrodes. *Biosens. Bioelectron.* **2010**, *25*, 2366–2369.
37. Matyba, P.; Yamaguchi, H.; Eda, G.; Chhowalla, M.; Edman, L.; Robinson, N. D. Graphene and Mobile Ions: The Key to All-Plastic, Solution-Processed Light-Emitting Devices. *ACS Nano* **2010**, *4*, 637–642.
38. Wu, J.; Agrawal, M.; Becerril, H. A.; Bao, Z.; Liu, Z.; Chen, Y.; Peumans, P. Organic Light-Emitting Diodes on Solution-Processed Graphene Transparent Electrodes. *ACS Nano* **2010**, *4*, 43–48.
39. Liu, Z.; Liu, Q.; Huang, Y.; Ma, Y.; Yin, S.; Zhang, X.; Sun, W.; Chen, Y. Organic Photovoltaic Devices Based on a Novel Acceptor Material: Graphene. *Adv. Mater.* **2008**, *20*, 3924–3930.
40. Guo, C.; Yang, H.; Sheng, Z.; Lu, Z.; Song, Q.; Li, C. Layered Graphene/Quantum Dots for Photovoltaic Devices. *Angew. Chem., Int. Ed.* **2010**, *49*, 1–5.
41. Yan, X.; Cui, X.; Li, B.; Li, L. Large, Solution-Processable Graphene Quantum Dots as Light Absorbers for Photovoltaics. *Nano Lett.* **2010**, *10*, 1869–1873.
42. Yang, N. L.; Zhai, J.; Wang, D.; Chen, Y. S.; Jiang, L. Two-Dimensional Graphene Bridges Enhanced Photoinduced Charge Transport in Dye-Sensitized Solar Cells. *ACS Nano* **2010**, *4*, 887–894.
43. Sun, S.; Gao, L.; Liu, Y. Enhanced Dye-Sensitized Solar Cell Using Graphene–TiO_2 Photoanode Prepared by Heterogeneous Coagulation. *Appl. Phys. Lett.* **2010**, *96*, 083113.
44. Tang, Y.; Lee, C.; Xu, J.; Liu, Z.; Chen, Z.; He, Z.; Cao, Y.; Yuan, G.; Song, H.; Chen, L.; *et al.* Incorporation of Graphenes in Nanostructured TiO_2 Films *via* Molecular Grafting for Dye-Sensitized Solar Cell Application. *ACS Nano* **2010**, *4*, 3482–3488.
45. Arco, L. G. D.; Zhang, Y.; Schlenker, C. W.; Ryu, K.; Thompson, M. E.; Zhou, C. Continuous, Highly Flexible, and Transparent Graphene Films by Chemical Vapor Deposition for Organic Photovoltaics. *ACS Nano* **2010**, *4*, 2865–2873.
46. Yin, Z.; Wu, S.; Zhou, X.; Huang, X.; Zhang, Q.; Boey, F.; Zhang, H. Electrochemical Deposition of ZnO Nanorods on Transparent Reduced Graphene Oxide Electrodes for Hybrid Solar Cells. *Small* **2010**, *6*, 307–312.
47. Wang, Y.; Chen, X.; Zhong, Y.; Zhu, F.; Loh, K. P. Large Area, Continuous, Few-Layered Graphene as Anodes in Organic Photovoltaic Devices. *Appl. Phys. Lett.* **2009**, *95*, 063302.
48. Wang, X.; Zhi, L.; Müllen, K. Transparent, Conductive Graphene Electrodes for Dye-Sensitized Solar Cells. *Nano Lett.* **2008**, *8*, 323–327.
49. Tung, V. C.; Chen, L.; Allen, M. J.; Wassei, J. K.; Nelson, K.; Kaner, R. B.; Yang, Y. Low-Temperature Solution Processing of Graphene–Carbon Nanotube Hybrid Materials for High-Performance Transparent Conductors. *Nano Lett.* **2009**, *9*, 1949–1955.
50. Eda, G.; Lin, Y.; Miller, S.; Chen, C.; Su, W.; Chhowalla, M. Transparent and Conducting Electrodes for Organic Electronics from Reduced Graphene Oxide. *Appl. Phys. Lett.* **2008**, *92*, 233305.
51. Wu, J.; Becerril, H. A.; Bao, Z.; Liu, Z.; Chen, Y.; Peumans, P. Organic Solar Cells with Solution-Processed Graphene Transparent Electrodes. *Appl. Phys. Lett.* **2008**, *92*, 263302.
52. Xu, Y.; Long, G.; Huang, L.; Huang, Y.; Wan, X.; Ma, Y.; Chen, Y. Polymer Photovoltaic Devices with Transparent Graphene Electrodes Produced by Spin-Casting. *Carbon* **2010**, *48*, 3308–3311.
53. Frank, O.; Tsoukleri, G.; Parthenios, J.; Papagelis, K.; Riaz, I.; Jalil, R.; Novoselov, K. S.; Galiotis, C. Compression Behavior of Single-Layer Graphenes. *ACS Nano* **2010**, *4*, 3131–3138.
54. Tsoukleri, G.; Parthenios, J.; Papagelis, K.; Jalil, R.; Ferrari, A. C.; Geim, A. K.; Novoselov, K. S.; Galiotis, C. Subjecting a Graphene Monolayer to Tension and Compression. *Small* **2009**, *5*, 2397–2402.
55. Li, X.; Zhu, Y.; Cai, W.; Borysiak, M.; Han, B.; Chen, D.; Piner, R. D.; Colombo, L.; Ruoff, R. S. Transfer of Large-Area Graphene Films for High-Performance Transparent Conductive Electrodes. *Nano Lett.* **2009**, *9*, 4359–4363.
56. Yu, T.; Ni, Z.; Du, C.; You, Y.; Wang, Y.; Shen, Z. Raman Mapping Investigation of Graphene on Transparent Flexible Substrate: The Strain Effect. *J. Phys. Chem. C* **2008**, *112*, 12602–12605.
57. Yamaguchi, H.; Eda, G.; Mattevi, C.; Kim, H.; Chhowalla, M. Highly Uniform 300 mm Wafer-Scale Deposition of Single and Multilayered Chemically Derived Gaphene Thin Films. *ACS Nano* **2010**, *4*, 524–528.
58. Blom, P. W. M.; Mihailetchi, V. D.; Koster, L. J. A.; Markov, D. E. Device Physics of Polymer: Fullerene Bulk Heterojunction Solar Cells. *Adv. Mater.* **2007**, *19*, 1551–1566.
59. Coakley, K. M.; McGehee, M. D. Conjugated Polymer Photovoltaic Cells. *Chem. Mater.* **2004**, *16*, 4533–4542.
60. Hummers, W. S.; Offeman, R. E. Preparation of Graphene Oxide. *J. Am. Chem. Soc.* **1958**, *80*, 1339.
61. Zhou, X.; Huang, X.; Qi, X.; Wu, S.; Xue, C.; Boey, F. Y. C.; Yan, Q.; Chen, P.; Zhang, H. *In Situ* Synthesis of Metal Nanoparticles on Single-Layer Graphene Oxide and Reduced Graphene Oxide Surfaces. *J. Phys. Chem. C* **2009**, *113*, 10842–10846.
62. Chen, X.; Mao, S. S. Titanium Dioxide Nanomaterials: Synthesis, Properties, Modifications, and Applications. *Chem. Rev.* **2007**, *107*, 2891–2959.